Bioresource Technology 200 (2016) 128–136

Contents lists available at ScienceDirect

Bioresource Technology

journal homepage: www.elsevier.com/locate/biortech

Investigating biofilm structure developing on carriers from lab-scale moving bed biofilm reactors based on light microscopy and optical coherence tomography

Chunyan Li [a], Simon Felz [a,b], Michael Wagner [c], Susanne Lackner [d], Harald Horn [a,e,*]

[a] Chair of Water Chemistry and Water Technology, Karlsruhe Institute of Technology, Engler-Bunte-Ring 9, 76131 Karlsruhe, Germany
[b] Department of Biotechnology, Faculty of Applied Sciences, Delft University of Technology, Julianalaan 67, 2628 BC Delft, The Netherlands
[c] Institute of Functional Interfaces, Karlsruhe Institute of Technology, Hermann-von-Helmholtz-Platz 1, 76344 Eggenstein-Leopoldshafen, Germany
[d] Urban Material Flow Management Technologies, Bauhaus-Institute for Infrastructure Solutions, Bauhaus University Weimar, Coudraystraße 7, 99421 Weimar, Germany
[e] DVGW Research Laboratories Water Chemistry and Water Technology, Engler-Bunte-Ring 9, 76131 Karlsruhe, Germany

HIGHLIGHTS

- 3D biofilm structure on MBBR carriers was visualized and quantified using OCT.
- Carrier geometry and aeration rate influence biofilm structure development.
- Correlation between biofilm structure characterized from 2D and 3D images.
- 3D imaging by means of OCT provides detailed biofilm structural information.

GRAPHICAL ABSTRACT

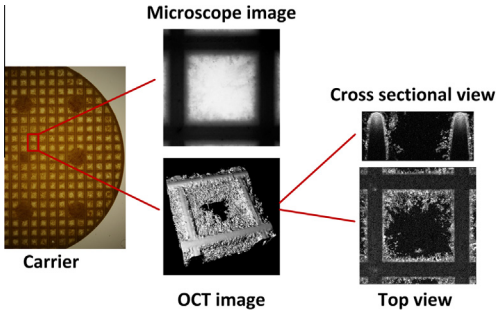

ARTICLE INFO

Article history:
Received 13 August 2015
Received in revised form 28 September 2015
Accepted 1 October 2015
Available online 13 October 2015

Keywords:
Moving bed biofilm reactor
Biofilm structure
Light microscopy
Optical coherence tomography
Structural parameter

ABSTRACT

This study focused on characterizing the structure of biofilms developed on carriers used in lab-scale moving bed biofilm reactors. Both light microscopy (2D) and optical coherence tomography (OCT) were employed to track the biofilm development on carriers of different geometry and under different aeration rates. Biofilm structure was further characterized with respect to average biofilm thickness, biofilm growth velocity, biomass volume, compartment filling degree, surface area, etc. The results showed that carriers with a smaller compartment size stimulated a quick establishment of biofilms. Low aeration rates favored fast development of biofilms. Comparison between the results derived from 2D and 3D images revealed comparable results with respect to average biofilm thickness and compartment filling degree before the carrier compartments were fully willed with biomass. However, 3D imaging with OCT was capable of visualizing and quantifying the heterogeneous structure of biofilms, which cannot be achieved using 2D imaging.

1. Introduction

Environmental conditions such as substrate availability and hydrodynamics might lead to various physical structures of biofilms, rough or smooth, porous or compact biofilms (Stoodley et al., 1999; Wagner et al., 2010). Therefore, different imaging

* Corresponding author at: Chair of Water Chemistry and Water Technology, Karlsruhe Institute of Technology, Engler-Bunte-Ring 9, 76131 Karlsruhe, Germany. Tel.: +49 72160842580; fax: +49 72160846497.
E-mail address: harald.horn@kit.edu (H. Horn).

http://dx.doi.org/10.1016/j.biortech.2015.10.013
0960-8524/

techniques have been introduced to investigate the physical structure as well as the biochemical properties, such as microscopy (Milferstedt et al., 2013), magnetic resonance imaging (MRI) (Manz et al., 2003; Neu et al., 2010), the mostly used confocal laser scanning microscopy (CLSM) (Lawrence and Neu, 1999), Raman microscopy (Ivleva et al., 2009) and scanning electron microscopy (Priester et al., 2007). Light microscopic images can cover large areas at the macro-scale. However, its application is limited by its low resolution. Studies of biofilm structure and function at the micro-scale have been advanced through CLSM, SEM etc. However, their applications are restricted by limited staining efficiency (CLSM), altering of biofilm structure due to drying (SEM), not being representative because of the small imaging area covered (CLSM, SEM).

According to Milferstedt et al. (2009), a characteristic length of at least 400 μm is required in biofilm images to provide relevant structural information, such as the impact of distance between colonies, on mass transport and detachment forces. This is the meso-scale from sub-millimeter to centimeter defined by Morgenroth and Milferstedt (2009). According to Wagner et al. (2010), MRI and optical coherence tomography (OCT) could be the optimal candidates for biofilm imaging at the meso-scale.

As a newly developed imaging technique in medical science (Huang et al., 1991), OCT has recently been introduced into biofilm research (Xi et al., 2006). The capability of OCT in the visualization and quantification of biofilm structure has been demonstrated by Xi et al. (2006) and Wagner et al. (2010). It compensates the aforementioned limitations and enables fast, *in situ* and non-invasive 3D visualization of biofilm structure at the meso-scale and thus exhibits high potential in biofilm research. One advantage worth emphasizing is that no biofilm preparation is required. Thereby, the structural integrity is well preserved. Derlon et al. (2012) characterized the structure of biofilms developed on the surface of gravity driven ultrafiltration system with respect to mean biofilm thickness, absolute and relative roughness by means of OCT. Janjaroen et al. (2013) investigated the mechanisms of *Escherichia coli* attachment onto biofilms fed with groundwater and successfully correlated the adhesion of *E. coli* cells to the physical structure of the biofilms. Compaction and de-compaction of biofilms under different permeate flux applied was observed by Dreszer et al. (2014) with OCT. Additionally, biofilm thickness calculated based on OCT images increased over time and was correlated with pressure drop and the biofilm resistance. However, all the quantifications in these studies were based only on 2D cross-sectional images. So far only Wagner et al. (2010) conducted 3D quantification of OCT images with respect to biofilm thickness and porosity for biofilm grown in a flume.

Moving bed biofilm reactors (MBBRs) incorporate plastic carriers into wastewater treatment process, thereby provide large protected surface area for microorganisms to attach and grow on. Most of the studies on MBBRs so far focused on optimizing its performance, such as the optimal filling degree (Gu et al., 2014), effect of carrier geometry (Levstek and Plazl, 2009) or microbial community structure (Zhang et al., 2013). There has been no study investigating the biofilm structure development on the carriers in MBBR yet.

The objective of the current study was to characterize the structure of biofilms developed on the carriers from lab-scale MBBRs based on light microscopic (2D) and OCT (3D) images. The results derived from 2D and 3D images were compared to examine the necessity of having complex 3D imaging. Moreover, the study intended to provide a scheme on how to image biofilms on MBBR carriers and to quantify their structure.

2. Methods

2.1. Reactor operation

Experiments were conducted in two lab-scale MBBRs. The reactors had an effective volume of 2.2 L. Each reactor was filled with two different types of carriers from AnoxKaldnes™, named Carrier A and Carrier B. The shape of the two types of carriers is similar to the widely used Chip M carrier from AnoxKaldnes. The characteristics of both carriers are provided in Table 1. Each reactor contained 190 carriers, 95 carriers of each type, resulting in a filling ratio of 13.6% and a total surface area of 0.213 m^2 (97 m^2 m^{-3}).

The pH value was maintained between 6.5 and 7.5 by a Wago unit using a 0.1 mol L^{-1} $KHCO_3$ solution. Compressed air supply was regulated by two air flow meters (Krohne DK 800/N) and supplied at the bottom of the reactor through perforated pipes installed on one side only.

Each reactor was inoculated for 24 h in batch mode with 2 L of activated sludge (total suspended solids (TSS) of 3.5 g L^{-1}) from the sewage plant in Neureut, Karlsruhe. Afterwards continuous operation started. The reactors were operated at room temperature (20 ± 1 °C) with a hydraulic retention time (HRT) of 4.4 h. The experiments were performed twice at different aeration rates, with a high aeration rate of 250 L h^{-1} (H, 39 days) and a low aeration rate of 150 L h^{-1} (L, 25 days). Temperature and pH values were measured on-line (Endress + Hauser Memosens CPS16D). Dissolved oxygen (DO) was measured daily with a DO meter (WTW Multi 350i). The experiments were terminated when all carriers were completely covered with biomass.

Cultivation medium was prepared twice a week according to Wagner et al. (2010). It consisted of 100–300 mg L^{-1} D-(+)-glucose H_2O, nutrients (in mg L^{-1}): $(NH_4)_2SO_4$ (20–40), $CaCl_2{\cdot}2H_2O$ (5.6–11.2), $MgSO_4{\cdot}7\ H_2O$ (14–28), $FeSO_4{\cdot}7\ H_2O$ (10–20), $NaNO_3$ (12–24), KH_2PO_4 (2.25–4.5), trace elements in (μg L^{-1}): H_3BO_3 (300–600), $CoSO_4{\cdot}7\ H_2O$ (130–260), $CuCl_2$ (8–16), $MnSO_4{\cdot}H_2O$ (20–40), $Na_2MoO_4{\cdot}2\ H_2O$ (26–52), $NiCl_2{\cdot}6\ H_2O$ (10–20), $ZnSO_4{\cdot}7\ H_2O$ (2–4). The concentrations were increased twice by 100% and 50% of the initial concentrations for COD and mineral medium, respectively. Concentrations of COD and nitrogen species (NH_4^+-N, NO_2^--N, NO_3^--N) in the reactor medium were measured with Hach-Lange Test Kit three times a week and once a week (NH_4^+-N, NO_2^--N, NO_3^--N), respectively.

2.2. Image acquisition

Images were acquired three times a week by means of light microscope (2D) and OCT (3D) from one carrier of each type and reactor. Inspection of three chips with light microscope showed no significant visual difference in biomass distribution. During image acquisition the carrier was immersed in filtered bulk liquid. The carriers were returned to the reactor after image acquisition.

2.2.1. Imaging with light microscope (2D)

2D images were taken using a light microscope SMT4 (Mikroskop Technik Rathenow) in combination with a DSLR camera (Canon EOS 600D). The camera setting was fixed at: 18 megapixel resolution, exposure time 1/10 s, ISO 100 and manual whitening balance. Magnification of the microscope was set at 16×, resulting in an image dimension of 8.5 × 5.7 mm^2 with a resolution of 611 pixels mm^{-1}.

To simplify image processing, only the full compartments were considered, neglecting the irregular ones. Thereby, 60% for Carrier A (including 62 compartments) and 70% for Carrier B (210 compartments) were imaged and quantified, respectively.

Table 1
Characteristics of the carrier material.

Carrier	Carrier thickness (mm)	Diameter (mm)	Compartment size (mm^2)	Comparments per carrier (–)	Protected surface area (cm^2)
A	1.05	30	2.4×2.4	103	8.84
B	1.05	30	1.4×1.4	300	13.63

2.2.2. Imaging with OCT (3D)

3D images were acquired using a Thorlabs Ganymede with a central wavelength of 930 nm and ThorImage 4.2 (Thorlabs GmbH, Dachau, Germany). The volume captured was $3.20 \times 3.20 \times 1.47\ mm^3$ ($450 \times 450 \times 700\ pixels^3$) for Carrier A and $3.30 \times 3.30 \times 1.47\ mm^3$ ($450 \times 450 \times 700\ pixels^3$) for Carrier B. Each image covered one and four compartments for Carrier A and B, respectively. Since biofilm consists of around 90% of water (Bakke et al., 2001), the refractive index was set to 1.33, the same as water. Three locations from border to center of the carrier were imaged on a single carrier. Images at the same position from both the top and bottom side of the carriers were taken to cover the whole depth of biofilm growing on the carriers.

2.3. Image analysis

Image analysis was carried out with Fiji software package (ImageJ 1.49g) (Schindelin et al., 2012) to extract structural information from the biofilm images. In the current study, only volumetric parameters were considered.

2.3.1. 2D light microscopic images

2D images were first converted to 8-bit grayscale images. The illumination correction method developed by Landini (2014) was applied to eliminate uneven illumination artifacts. Contrast enhancement was implemented prior to automatic thresholding. Finally, the resulting binarized images had intensity values of 1 for biofilm and 0 for the void area in the center of the compartment. Measurement of the void area was performed by Fiji 'analyze particles' plugin.

Quantification of the biofilm structure based on 2D images is illustrated in Fig. 1(a), with respect to average biofilm thickness ($\bar{L}_{f,2D}$) (Murga et al., 1995), compartment coverage (η_{2D}) and surface enlargement (SE_{2D}) (Picioreanu et al., 1997). Detailed definitions are:

- Average biofilm thickness ($\bar{L}_{f,2D}$): calculated by converting the area of the empty space free of biomass A_V into an equivalent square of the same area. The distance between the border of the compartment and the border of the empty square gives $\bar{L}_{f,2D}$:

$$\bar{L}_{f,2D} = \frac{a_0 - \sqrt{A_v}}{2} \quad [mm]$$

- Biofilm growth velocity ($u_{f,2D}$): the time derivative of $\bar{L}_{f,2D}$. A positive value indicates growth of biofilm, while a negative value implies detachment of biofilm.

$$u_{f,2D} = \frac{\bar{L}_{f,2D}(i + \Delta t) - \bar{L}_{f,2D}(i)}{day(i + \Delta t) - day(i)} \quad [mm \cdot d^{-1}]$$

where i and Δt denote the day and the time difference between two measurements, respectively.

- Compartment coverage (η_{2D}): percentage of biofilm area to the total area of one compartment (A_{tot}). This value represents the coverage of a carrier by biofilm.

$$\eta_{2D} = \frac{A_b}{a_0^2} \cdot 100 \quad [\%]$$

- Surface enlargement (SE_{2D}) (Picioreanu et al., 1997): ratio of the length of biofilm front (p_b) to the substratum length (p_0). It also indirectly measures the heterogeneity of the biofilm surface.

$$SE_{2D} = \frac{p_b}{p_0} \quad [-]$$

2.3.2. 3D OCT images

Fig. 1(b) presents the procedure for 3D image analysis. To facilitate the comparison, the images were cut to the same size first, one and four compartment(s) for Carrier A and B, respectively. The images were converted to 8-bit grayscale images. Brightness and contrast was adjusted manually to achieve the best signal-to-noise ratio. During image acquisition, the carriers were slightly bent, which resulted in tilted images. To facilitate the following processing, the images were subjected to a tiltness correction. Then, the beams of the carriers were outlined and removed. "Gaussian Blur 3D" and automatic thresholding embedded in Fiji were applied to separate the biomass from the background.

A representation of the whole depth of the biofilms was achieved by concatenating the image stacks from top and bottom view, with each part contributing 60% and 40% to the whole carrier depth, respectively. Isolated noise was removed by the "find connected regions" plugin (Longair, 2012). Subsequently the biofilm surface was measured with the "BoneJ Isosurface" plugin (Doube et al., 2010). In the end, all white pixels in the whole stack were summed to represent the amount of biomass.

Quantification of biofilm structure based on 3D datasets was conducted with respect to the following parameters:

- Average biofilm thickness ($\bar{L}_{f,3D}$) (Murga et al., 1995): The 3D dataset was firstly resliced to obtain top view images (xy plane). The average biofilm thickness was calculated for each slice (495 slices in total) in the same way to calculate $\bar{L}_{f,2D}$. The values were averaged over the number of slices, resulting in $\bar{L}_{f,3D}$.
- Biofilm growth velocity ($u_{f,3D}$): similar to the calculation of $u_{f,2D}$.

$$u_{f,3D} = \frac{\bar{L}_{f,3D}(i + \Delta t) - \bar{L}_{f,3D}(i)}{day(i + \Delta t) - day(i)} \quad [mm \cdot d^{-1}]$$

- Compartment filling degree (η_{3D}): calculated as the ratio between voxels of biomass and the total number of voxels of a blank compartment.

$$\eta_{3D} = \frac{\text{total number of white voxels (biofilm)}}{\text{total number of voxels (blank)}} \cdot 100 \quad [\%]$$

- Biomass volume (BV_{tot}) (Heydorn et al., 2000): reflects the total amount of biomass on the whole carrier. It was calculated differently for Carrier A and B (see Table 1) due to the different sizes of the compartments as well as the total coverage of the carriers.

$$BV_{A,tot} = BV_{3D} \cdot 62 \cdot \frac{100}{60} \quad [mm^3]$$

$$BV_{B,tot} = BV_{3D} \cdot 210 \cdot \frac{100}{70} \quad [mm^3]$$

$$\text{with } BV_{3D} = \eta_{3D} \cdot \text{volume of one compartment} \quad [mm^3]$$

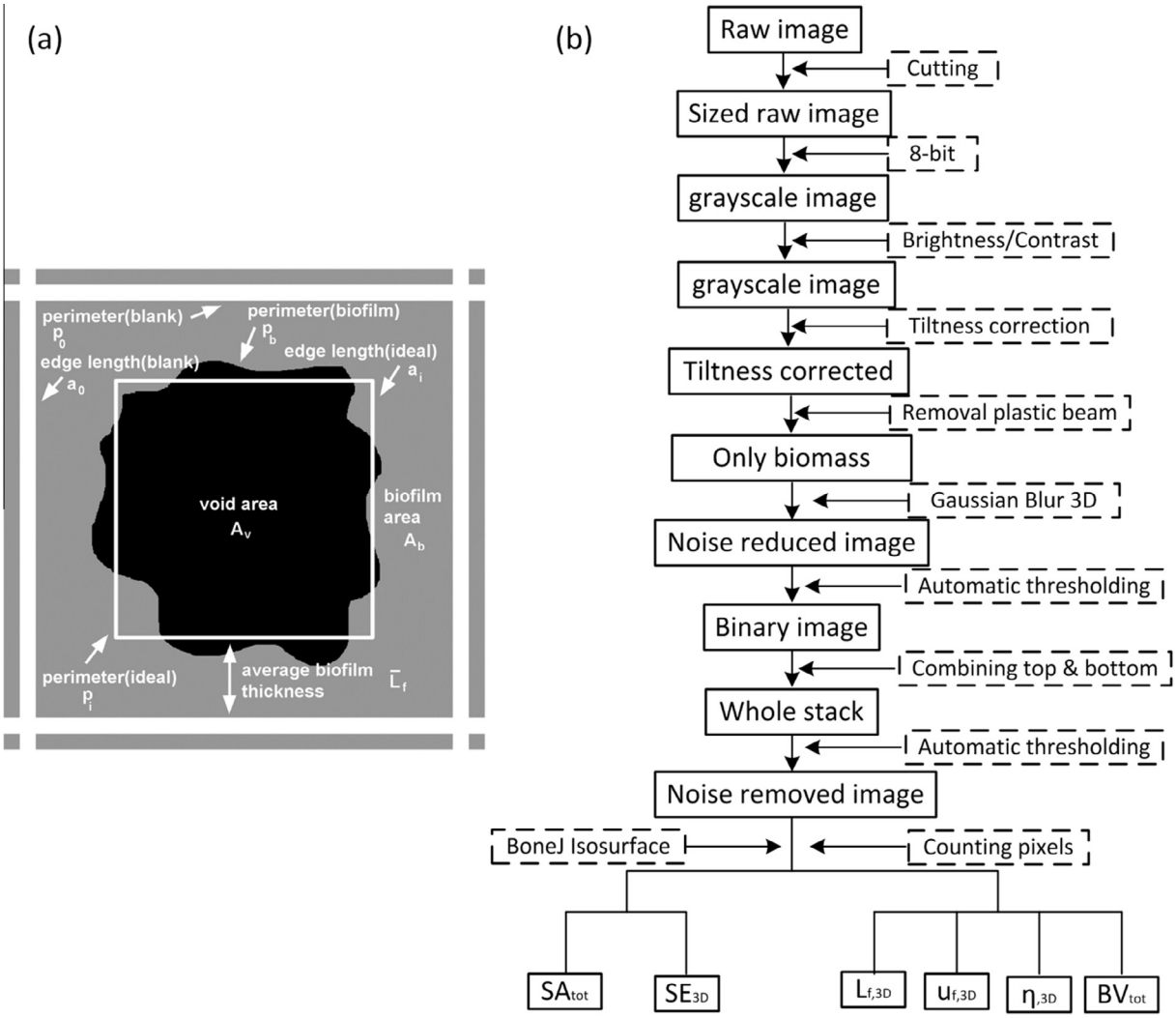

Fig. 1. (a) Schematic of the calculation of 2D parameters based on light microscopic images and (b) the procedure for 3D image processing based on OCT images. (a) The white thick lines define the boundary of one compartment. Biofilm is presented in gray. The void area in a compartment is presented in black. (b) The closed rectangular are the images for the next step. The open rectangular are the image processing steps.

- Surface area (SA_{tot}): the area of the biofilm-liquid interface, measured by the "BoneJ Isosurface" plugin.

$$SA_{A,tot} = SA_{3D} \cdot 62 \cdot \frac{100}{60} \quad [cm^2]$$

$$SA_{B,tot} = SA_{3D} \cdot 210 \cdot \frac{100}{70} \quad [cm^2]$$

- Surface enlargement (SE_{3D}): similar to SE_{2D}, it was calculated by dividing biofilm surface area by the area of a blank carrier.

$$SE_{3D} = \frac{SA_{3D}(biofilm)}{SA_{3D}(blank)} \quad [-]$$

3. Results and discussion

3.1. Reactor operation

During the reactor operation with high and low aeration rates, the operation parameters were in the expected range (Table 2). Reactor performance was evaluated with respect to COD turnover ($g\,d^{-1}$). Influent COD was increased for both aeration rates from 100 to 300 $mg\,L^{-1}$. The average COD turnover for both high and low aeration rates was 1.96 $g\,d^{-1}$ and 2.00 $g\,d^{-1}$, respectively (see Table 2). Nevertheless, the MBBRs were simply used for the cultivation of biofilms on the carriers. The focus was given to biofilm imaging and biofilm structure analysis.

3.2. Visualization of biofilm structure on carriers

The biofilm images obtained from both light microscopy and OCT showed that biofilm grew from the carrier walls toward the center of the compartment, with more biomass in the corners. As OCT is capable of acquiring 3D image data, cross-sectional image revealed that there was more biomass at the vertical center of the carrier and less biomass at the tip of the plastic beams, which formed a funnel-like structure. Similar funnel-like biofilm structure was also observed by Almstrand et al. (2014) with cryosectioning and assembled FISH images on the mini-chips used for Anammox bacteria in MBBR. However, the biofilm structure was obtained only for the first 400 μm out of the 2 mm depth of the whole carrier (Almstrand et al., 2014). In this study OCT enabled us to investigate the 3D biofilm structure non-invasively over the whole depth of the carriers. Such pattern of biomass distribution inside the compartments of the carriers is presumably controlled by collision of the carriers against each other as well as detachment induced by shear forces.

Table 2
Reactor operation parameters.

	Duration (d)	pH (–)	T (°C)	DO (mg L^{-1})	HRT (h)	Average COD removal (g d^{-1})	α (%)
High	39	6.9 ± 0.2	21.2 ± 0.6	7.1 ± 0.3	4.1 ± 0.4	1.96	58
Low	25	6.9 ± 0.3	21.7 ± 0.5	7.6 ± 0.3	4.4 ± 0.2	2.00	55

α: average COD removal efficiency.

3.3. Comparison of biofilm structure on Carrier A and B

Various types of carriers are available on the market for MBBR processes. The study of Levstek and Plazl (2009) with two carriers of fundamentally different geometries failed to conclude the influence of carrier geometry on carrier performance. So far it is still not clear how the carrier geometry affects biofilm growth. In this study the influence of carrier geometry on biofilm structure development was investigated with respect to $\bar{L}_{f,3D}$, BV_{3D} and η_{3D} and SA_{tot}, presented in Fig. 2. The results are the average values over the three imaging locations to consider the carrier as a whole to investigate the temporal development of biofilm structure. The indices A and B refer to Carrier A and B, respectively. Due to the difference in compartment size and substratum area, a direct comparison of BV_{3D} and SA_{3D} between A and B would not lead to any meaningful conclusion. Instead BV_{3D} and SA_{3D} were converted to values for the entire carrier and then compared, as the two carriers have the same dimension.

From Fig. 2(a)–(c), it is clear that the average biofilm thickness ($\bar{L}_{f,3D}$), compartment filling degree (η_{3D}) and biomass volume (BV_{3D}) advanced gradually as expected with biofilm growth for both Carrier A and B. Different from the calculation of $\bar{L}_{f,3D}$ by counting the biomass pixels, the development of biofilm surface area (SA_{3D}) showed different trend. The growth of heterogeneous biofilms at the early phase increased SA_{3D} for both types of carriers. However, after the biofilm joined from center, further growth of biofilms led to decrease of SA_{3D}.

Although the general trend in biofilm structure development was similar, difference in biofilm structure can be easily distinguished between the two types of carriers. From Fig. 2(a), Carrier B had slightly higher values for $\bar{L}_{f,3D}$, η_{3D}, and BV_{tot} than Carrier A until day 11. This suggests that Carrier B promoted quicker initial establishment of biofilms. Compared to Carrier A, Carrier B provided more protected surface area for biofilm to grow on (see Table 1). After the compartments were fully filled with biomass on day 11 for Carrier B, $\bar{L}_{f,3D}$, η_{3D}, and BV_{tot} kept relatively constant. Since the compartments of Carrier A are larger, the biofilm grew further, with $\bar{L}_{f,3D}$, and BV_{tot} exceeding the corresponding values of Carrier B. Nevertheless, $\eta_{3D,B}$ was always higher than $\eta_{3D,A}$ (see Fig. 2(b)), indicating that the compartments of Carrier A were not fully filled by biofilm until the end of the reactor operation. The smaller compartment size of Carrier B promoted quick initial biofilm growth. Nevertheless, the amount of biomass accumulated on both types of carriers was comparable, see Fig. 2(c). Shown in Fig. 2(d), biofilm surface area $SA_{tot,B}$ reached its maximum on day 4 and was significantly higher than $SA_{tot,A}$. Afterwards $SA_{tot,B}$

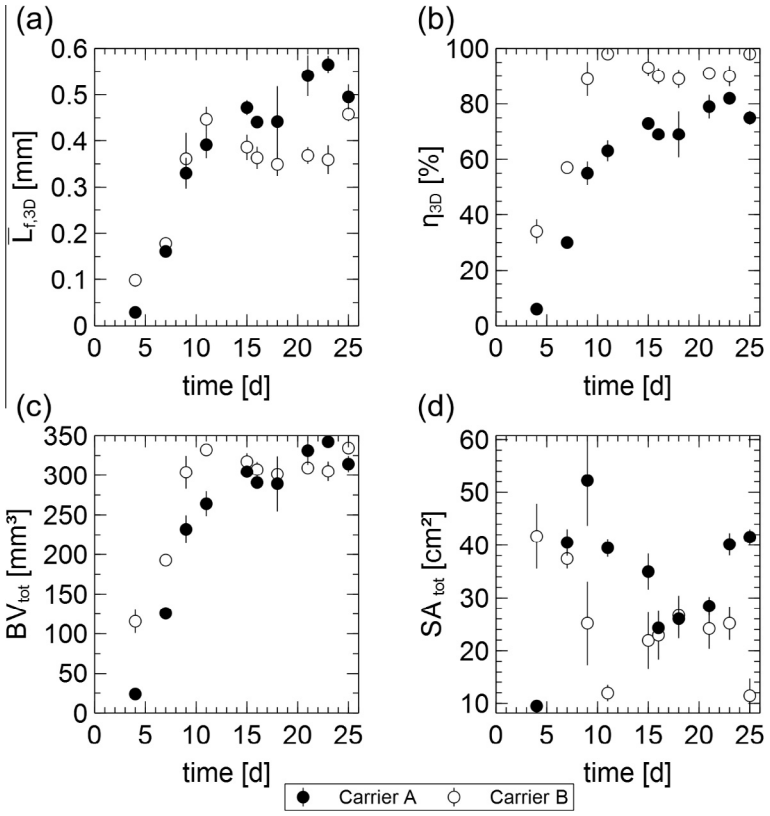

Fig. 2. The influence of carrier geometry on biofilm structure development. Parameters shown for Carrier A and B include (a) average biofilm thickness ($\bar{L}_{f,3D}$), (b) compartment filling degree (η_{3D}), (c) total biomass volume (BV_{tot}) and (d) total surface area (SA_{tot}).

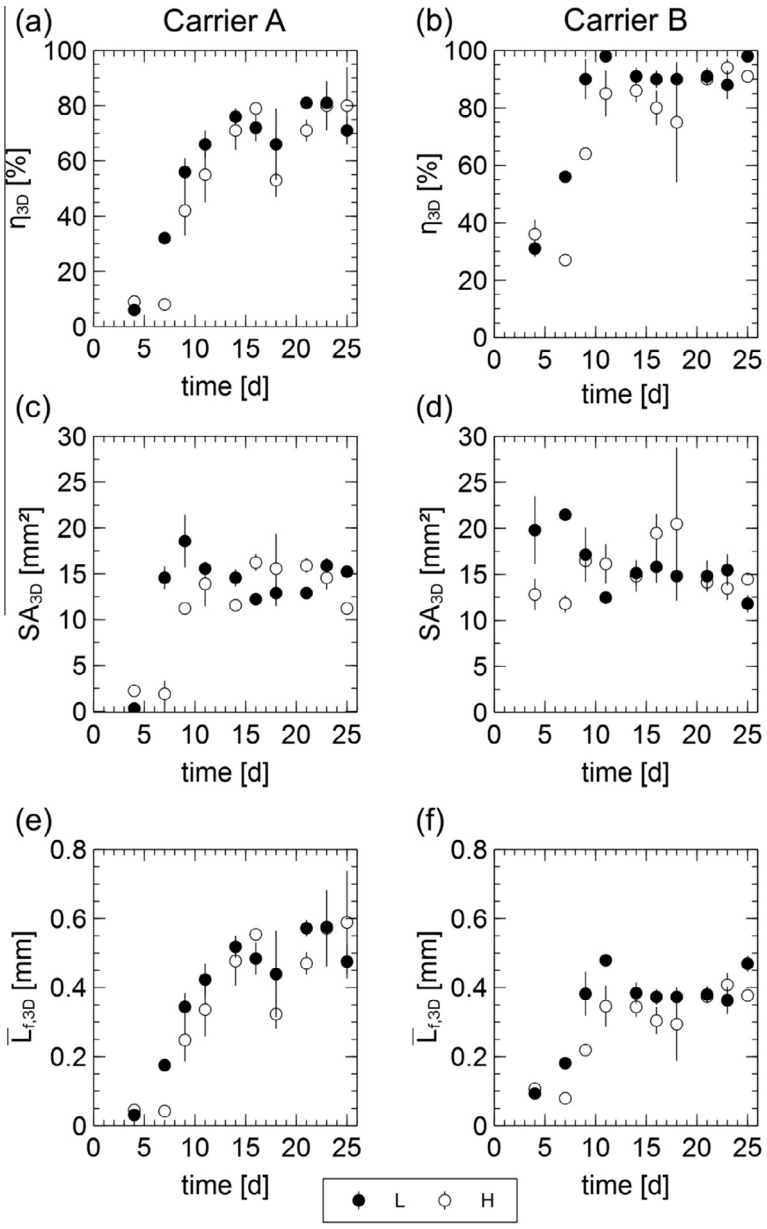

Fig. 3. The effect of aeration rate on biofilm structure with respect to compartment filling degree (η_{3D}), surface area (SA_{3D}) and growth rate ($u_{F,3D}$) for Carrier A (a), (c), (e) and Carrier B (b), (d) and (f) respectively.

decreased continuously until day 11 and approached a relatively stable value of around 25 cm^2 between days 15 and 23. $SA_{tot,A}$ increased sharply from day 4 onwards and exceeded $SA_{tot,B}$ on day 7. Decrease in SA_{tot} was also valid for Carrier A.

Boltz and Daigger (2010) pointed out that excessive growth of biofilm would lead to reduction of biofilm surface area, which is also valid for the inward growth of biofilm in the carriers used here, see Fig. 2(d). However, contrary to the expected continuing decrease, SA_{3D} increased in the end. Except erosion and detachment that lead to loss of biomass, a sudden decrease in $\bar{L}_{f,3D}$, BV_{3D} and η_{3D} from day 23 to day 25 can partly be attributed to the limitation in penetration depth of OCT. Similar limitation has also been observed in the application of OCT for biofilm related research reported by Derlon et al. (2012) and Dreszer et al. (2014). Light is attenuated due to the strong reflection at the air–water interface and scattering in biofilms because of the difference in the refractive index between biomaterial and water (Zhu et al., 2013). Therefore, no information could be gathered at deeper biofilm layer. Different from the treatment in Dreszer et al. (2014) to fill the false void, the voids were not artificially filled in the current study, which directly led to the underestimation of the parameters calculated based on voxel counting, such as $\bar{L}_{f,3D}$, BV_{3D} and η_{3D}. On the contrary, the ISO surface plugin of BoneJ sums up all the surface area available without distinguishing between the external and internal surface. The presence of such false voids enlarges the total surface area, thereby leading to an overestimation of the bulk-biofilm interface. To overcome such limitations, it might be helpful to use OCT with longer wavelength (Kodach et al., 2010) and/or a stronger power source, to treat biofilms using optical clearing agents (Larina et al., 2008) or work with water immersion lens that can be used under water surface.

3.4. The influence of aeration rate on biofilm structure

Agitation of the carriers in our study was achieved through aeration. By varying the aeration intensity, the movement of the car-

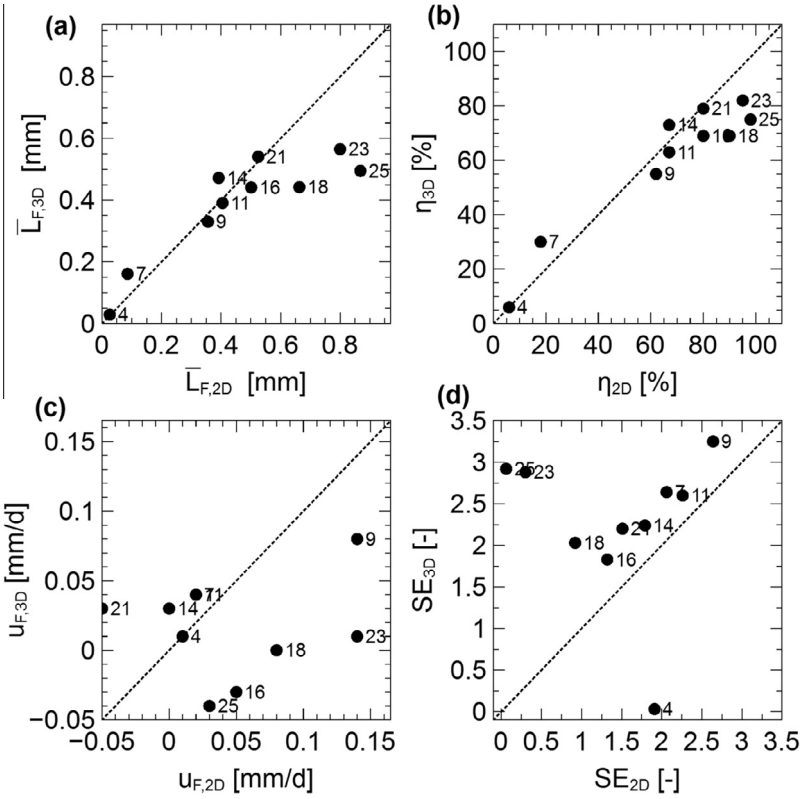

Fig. 4. Correlation between the quantification based on stereomicroscopy and OCT images with respect to (a) average biofilm thickness ($\bar{L}_f$), (b) compartment fill degree (η), (c) biofilm growth rate u_F and (d) surface enlargement (SE). The diagonal line represents a perfect correlation between the two variables plotted. The numbers label the day of the measurement.

riers varied, resulting in changes of hydrodynamics in the reactor. Therefore, evolution of different biofilm structures was expected. During the experiment with a high aeration rate, OCT images were acquired only from one side of the carrier. Therefore, all the comparison in this section is based on results derived from 60% of the carrier height for both types of carriers. The comparison with respect to η_{3D}, SA_{3D} and $\bar{L}_{f,3D}$ is presented in Fig. 3. The compartment filling degree η_{3D} at a low aeration rate was slightly higher than that at high aeration rates for both types of carrier (Fig. 3 (a) and (b)). Larger differences between low and high aeration rates were observed for biofilms at an early phase before day 11. For young biofilms (younger than 11 days) on both carriers, low aeration rates resulted in fast biomass accumulation. The difference narrowed down with biofilm growth and became insignificant when η_{3D} reached relatively stable levels.

For biofilm surface area SA_{3D} (for a single compartment), the influence of aeration rate can be separated into two phases, see Fig. 3(c) and (d). For young biofilms (<11 day) on both carriers, low aeration rates resulted in fast biomass accumulation thereby boosting SA_{3D}. High aeration rates led to low biofilm surface area. After day 11 the discrepancy in SA_{3D} diminished, while SA_{3D} kept relatively constant. The average biofilm thickness $\bar{L}_{f,3D}$ was always higher at low aeration rates compared to the results at high aeration rates, for both carrier geometries (Fig. 3(e) and (f)). Although growing slower, SA_{3D} at high aeration rates enlarged steadily without decreasing trend. It is speculated that high aeration rates boosted fast movement of carriers in the reactor. Thereby, the carriers experienced higher shear forces. This led to the formation of smooth and compact biofilms, which is in accordance to the results of Liu and Tay (2002).

Despite the slight difference in biofilm structure between the low and high aeration rate at the beginning, the difference diminished when the carriers were filled with biomass. Referring to the reactor performance, the difference in COD removal in the end was comparable, which is probably due to non-limiting DO concentrations above 7 mg L^{-1} at both aeration rates (Rahimi et al., 2011). This implies that an aeration rate as high as 250 L h^{-1} did not necessarily improve COD removal (see Table 2). On the contrary, energy could be saved providing relatively lower aeration rate.

3.5. Correlation between 2D and 3D structural parameters

Imaging with light microscopy can provide a quick impression and overview of the biofilms developed on carriers. As a similar parameter set has been used to characterize biofilm structure based on both 2D and 3D images, the results were compared with respect to biofilm thickness ($\bar{L}_f$), growth velocity (u_f), compartment filling degree (η) and surface enlargement (SE). The results are presented in Fig. 4, with the same parameter pair plotted in one plot. The closer the points are to the diagonal, the clearer the correlation between the results calculated from the two types of images.

In Fig. 4(a), $\bar{L}_{f,2D}$ was compared with $\bar{L}_{f,3D}$. The points lying above the dashed line imply a $\bar{L}_{f,3D}$ greater than $\bar{L}_{f,2D}$, and *vice versa*. Most of the points lie close to the diagonal, which indicates that the average biofilm thicknesses based on 2D and 3D images were close to each other, with $\bar{L}_{f,3D} = 0.5442 * \bar{L}_{f,2D} + 0.1352$ ($R^2 = 0.76$). While on days 18, 23 and 25, $\bar{L}_{f,2D}$ were greater than $\bar{L}_{f,3D}$. As the calculation of η was similar to $\bar{L}_f$, the distribution of points for η (see Fig. 4 (b)) shows similar pattern as $\bar{L}_f$, with the majority of the points spreading along the diagonal and $\eta_{3D} = 0.7358 * \eta_{2D} + 11.3$ ($R^2 = 0.90$). As has been described that biofilms develop funnel-like structure with more biomass in the vertical center of the carrier and less biomass close to the two faces of the carrier. Before the compartments were blocked by biomass from the vertical center, the average biofilm thickness $\bar{L}_f$ and compartment filling

degree η showed no significant difference between the results based on 2D and 3D images. However, after the compartments were completely filled after day 21, 2D imaging could not capture the structural differences anymore. 3D imaging with OCT could capture the further change in biofilm structure. Light microscopy was limited due to the projection of 3D heterogeneous structure over the depth of the carriers. Therefore, the values for $\bar{L}_f$ and η on day 23 and 25 scattered further from the diagonal.

The points of biofilm growth velocity (u_F) in Fig. 4(c) for the operation in the early phase (day 4–14) were along the diagonal. Afterwards the points spread widely apart from (mostly below) the diagonal, which implies higher biofilm growth velocity calculated from 2D images. The points in Fig. 4(d) on SE all lay above the diagonal except on day 4, which infers that the surface enlargement based on 3D image dataset was always higher than that based on 2D images. SE measures biofilm surface heterogeneity. OCT images were capable of capturing detailed 3D hills and valleys at the biofilm surface. Projection of such 3D structure onto a 2D plane led to loss of information, thereby a reduction of surface heterogeneity. The two measurements on day 23 and 25 in Fig. 4 (d) can be attributed to the blockage of the carrier compartments resulting in SE_{2D} approaching 0.

Comparison between the results extracted from 2D and 3D images suggests that 2D analysis could replace the 3D analysis to monitor the overall biofilm growth with respect to the development of the average biofilm thickness and carrier compartments filling degree before the compartments were completely filled with biomass. Another advantage of 2D imaging lies in the larger coverage allowing more area to be included in the quantification. However, 2D imaging cannot replace 3D imaging when the heterogeneous surface structure is of concern, such as surface enlargement. The study of Zielinski et al. (2012) also showed the superior accuracy of 3D over 2D analysis for CLSM images. OCT provided more detailed information on biomass distribution inside the compartment as well as the heterogeneous 3D biofilm surface structure, which could not be captured by 2D imaging. While light microscopy only revealed the overall structural information of a compartment, OCT could explicitly visualize local variation of biofilm growth and provide more descriptive information on biofilm structure by 3D structure analysis.

4. Conclusions

In summary, OCT revealed 3D funnel-like biofilm structure inside the carriers used in lab-scale MBBRs. The carriers with small compartment size promoted quick biofilm growth. The carriers with big compartment size reached higher biofilm surface area after the carriers were filled. Low aeration rate allowed fast biofilm development and higher compartment filling degree on both types of carriers. Comparison of the imaging techniques revealed strong correlation for $\bar{L}_f$ and η between 2D and 3D images. However, 3D imaging with OCT provided more descriptive information on biofilm structure, such as the distribution of biomass, biomass volume and biofilm surface area.

Acknowledgements

The authors acknowledge the support of AnoxKaldnes. Financial support from the Water Science Alliance of The Helmholtz Associations is acknowledged too.

Appendix A. Supplementary data

Supplementary data associated with this article can be found, in the online version, at http://dx.doi.org/10.1016/j.biortech.2015.10.013.

References

Almstrand, R., Persson, F., Daims, H., Ekenberg, M., Christensson, M., Wilén, B.-M., Sörensson, F., Hermansson, M., 2014. Three-dimensional stratification of bacterial biofilm populations in a moving bed biofilm reactor for nitritation–anammox. Int. J. Mol. Sci. 15 (2), 2191–2206.

Bakke, R., Kommedal, R., Kalvenes, S., 2001. Quantification of biofilm accumulation by an optical approach. J. Microbiol. Methods 44 (1), 13–26.

Boltz, J.P., Daigger, G.T., 2010. Uncertainty in bulk-liquid hydrodynamics and biofilm dynamics creates uncertainties in biofilm reactor design. Water Sci. Technol. 61 (2), 307–316.

Derlon, N., Peter-Varbanets, M., Scheidegger, A., Pronk, W., Morgenroth, E., 2012. Predation influences the structure of biofilm developed on ultrafiltration membranes. Water Res. 46 (10), 3323–3333.

Doube, M., Kłosowski, M.M., Arganda-Carreras, I., Cordelières, F.P., Dougherty, R.P., Jackson, J.S., Schmid, B., Hutchinson, J.R., Shefelbine, S.J., 2010. BoneJ: Free and extensible bone image analysis in ImageJ. Bone 47 (6), 1076–1079.

Dreszer, C., Wexler, A.D., Drusová, S., Overdijk, T., Zwijnenburg, A., Flemming, H.-C., Kruithof, J.C., Vrouwenvelder, J.S., 2014. In-situ biofilm characterization in membrane systems using smation, structure, detachment and impact of flux change. Water Res. 67, 243–254.

Gu, Q., Sun, T., Wu, G., Li, M., Qiu, W., 2014. Influence of carrier filling ratio on the performance of moving bed biofilm reactor in treating coking wastewater. Bioresour. Technol. 166, 72–78.

Heydorn, A., Nielsen, A.T., Hentzer, M., Sternberg, C., Givskov, M., Ersbøll, B.K., Molin, S., 2000. Quantification of biofilm structures by the novel computer program COMSTAT. Microbiology 146, 2395–2407.

Huang, D., Swanson, E., Lin, C., Schuman, J., Stinson, W., Chang, W., Hee, M., Flotte, T., Gregory, K., Puliafito, C., 1991. Optical coherence tomography. Science 254 (5035), 1178–1181.

Ivleva, N.P., Wagner, M., Horn, H., Niessner, R., Haisch, C., 2009. Towards a nondestructive chemical characterization of biofilm matrix by Raman microscopy. Anal. Bioanal. Chem. 393 (1), 197–206.

Janjaroen, D., Ling, F., Monroy, G., Derlon, N., Mogenroth, E., Boppart, S.A., Liu, W.-T., Nguyen, T.H., 2013. Roles of ionic strength and biofilm roughness on adhesion kinetics of *Escherichia coli* onto groundwater biofilm grown on PVC surfaces. Water Res. 47 (7), 2531–2542.

Kodach, V.M., Kalkman, J., Faber, D.J., van Leeuwen, Ton.G., 2010. Quantitative comparison of the OCT imaging depth at 1300 nm and 1600 nm. Biomed. Opt. Exp. 1 (1), 176–185.

Landini, G., 2014. How to correct background illumination in brightfield microscopy. <http://imagejdocu.tudor.lu/doku.php?id=howto:working:how_to_correct_background_illumination_in_brightfield_microscopy> (accessed 15 May 2014).

Larina, I.V., Carbajal, E.F., Tuchin, V.V., Dickinson, M.E., Larin, K.V., 2008. Enhanced OCT imaging of embryonic tissue with optical clearing. Laser Phys. Lett. 5 (6), 476–479.

Lawrence, J.R., Neu, T.R., 1999. Confocal laser scanning microscopy for analysis of microbial biofilms. In: Biofilms, vol. 310. Elsevier, pp. 131–144.

Levstek, M., Plazl, I., 2009. Influence of carrier type on nitrification in the moving-bed biofilm process. Water Sci. Technol. 59 (5), 875–882.

Liu, Y., Tay, J.-H., 2002. The essential role of hydrodynamic shear force in the formation of biofilm and granular sludge. Water Res. 36 (7), 1653–1665.

Longair, M., 2012. Find Connected Regions: PlugIn for ImageJ. <http://www.longair.net/edinburgh/imagej/find-connected-regions/> (accessed 29 July 2013).

Manz, B., Volke, F., Goll, D., Horn, H., 2003. Measuring local flow velocities and biofilm structure in biofilm systems with magnetic resonance imaging (MRI). Biotechnol. Bioeng. 84 (4), 424–432.

Milferstedt, K., Pons, M.-N., Morgenroth, E., 2009. Analyzing characteristic length scales in biofilm structures. Biotechnol. Bioeng. 102 (2), 368–379.

Milferstedt, K., Santa-Catalina, G., Godon, J.-J., Escudié, R., Bernet, N., 2013. Disturbance frequency determines morphology and community development in multi-species biofilm at the landscape scale. PLoS ONE 8 (11), e80692.

Morgenroth, E., Milferstedt, K., 2009. Biofilm engineering: linking biofilm development at different length and time scales. Rev. Environ. Sci. Biotechnol. 8 (3), 203–208.

Murga, R., Stewart, P.S., Daly, D., 1995. Quantitative analysis of biofilm thickness variability. Biotechnol. Bioeng. 45, 503–510.

Neu, T.R., Manz, B., Volke, F., Dynes, J.J., Hitchcock, A.P., Lawrence, J.R., 2010. Advanced imaging techniques for assessment of structure, composition and function in biofilm systems. FEMS Microbiol. Ecol. 72 (1), 1–21.

Picioreanu, C., van Loosdrecht, M., Heijnen, J.J., 1997. Mathematical modeling of biofilm structure with a hybrid differential-discrete cellular automaton approach. Biotechnol. Bioeng. 58, 101–116.

Priester, J.H., Horst, A.M., de Werfhorst, Van., Laurie, C., Saleta, J.L., Mertes, L.A.K., Holden, P.A., 2007. Enhanced visualization of microbial biofilms by staining and environmental scanning electron microscopy. J. Microbiol. Methods 68 (3), 577–587.

Rahimi, Y., Torabian, A., Mehrdadi, N., Habibi-Rezaie, M., Pezeshk, H., Nabi-Bidhendi, G.R., 2011. Optimizing aeration rates for minimizing membrane fouling and its effect on sludge characteristics in a moving bed membrane bioreactor. J. Hazard. Mater. 186 (2–3), 1097–1102.

Schindelin, J., Arganda-Carreras, I., Frise, E., Kaynig, V., Longair, M., Pietzsch, T., Preibisch, S., Rueden, C., Saalfeld, S., Schmid, B., Tinevez, J.-Y., White, D.J.,

Hartenstein, Eliceiri, K., Tomancak, P., Cardona, A., . Fiji: an open-source platform for biological-image analysis. Nat. Methods 9 (7), 676–682.
Stoodley, P., Boyle, J.D., De Beer, D., Lappin-Scott, H.M., 1999. Evolving perspectives of biofilm structure. Biofouling 14 (1), 75–90.
Wagner, M., Taherzadeh, D., Haisch, C., Horn, H., 2010. Investigation of the mesoscale structure and volumetric features of biofilms using optical coherence tomography. Biotechnol. Bioeng. 107 (5), 844–853.
Xi, C., Marks, D., Schlachter, S., Luo, W., Boppart, S.A., 2006. High-resolution three-dimensional imaging of biofilm development using optical coherence tomography. J. Biomed. Opt. 11 (3), 034001(1-6).
Zhang, S., Wang, Y., He, W., Xing, M., Wu, M., Yang, J., Gao, N., Sheng, G., Yin, D., Liu, S., 2013. Linking nitrifying biofilm characteristics and nitrification performance in moving-bed biofilm reactors for polluted raw water pretreatment. Bioresour. Technol. 146, 416–425.
Zhu, D., Larin, K.V., Luo, Q., Tuchin, V.V., 2013. Recent progress in tissue optical clearing. Laser Photon. Rev. 7 (5), 732–757.
Zielinski, J.S., Zielinska, A.K., Bouaynaya, N. (Eds.), 2012. Three-dimensional morphology quantification of biofilm structures from confocal laser scanning microscopy images. In: International Conference on Industrial and Intelligent Information (ICIII 2012). Singapore. March 17–18.